Materials Today Bio 13 (2022) 100189

Contents lists available at ScienceDirect

Materials Today Bio

journal homepage: www.journals.elsevier.com/materials-today-bio

Cascade targeting codelivery of ingenol-3-angelate and doxorubicin for enhancing cancer chemoimmunotherapy through synergistic effects in prostate cancer

Zhicheng Wang [a,1], Chao Sun [d,1], Haijun Wu [e], Jizhen Xie [e], Tong Zhang [a], Yumin Li [a], Xuelian Xu [a], Peilin Wang [b,**], Cheng Wang [a,c,*]

[a] Key Laboratory of Marine Drugs, Chinese Ministry of Education, School of Medicine and Pharmacy, Ocean University of China, Qingdao, 266003, PR China
[b] Department of General Surgery, The Second Hospital of Shandong University, Ji'nan, 250033, PR China
[c] Laboratory for Marine Drugs and Bioproducts, Pilot National Laboratory for Marine Science and Technology, Qingdao, 266237, PR China
[d] Central Research Laboratory, The Second Hospital of Shandong University, Ji'nan, 250033, PR China
[e] Shandong Center for Food and Drug Evaluation and Inspection, Ji'nan, 250013, PR China

ARTICLE INFO

Keywords:
Anti-angiogenesis
Ingenol-3-angelate
Immunogenic cell death
Mitophagy
Chemoimmunotherapy
Nanoparticles

ABSTRACT

Immunotherapy has led to an expansion of the treatment of malignancies, but its effect in prostate cancer (PCa) patients is modest. Chemoimmunotherapy is a promising approach that has attracted substantial attention. Although the widely used clinical chemotherapeutic drug doxorubicin (DOX) elicits immunogenic cell death (ICD), its weak ICD effect and the abnormal vasculature of tumors severely limit its efficacy in chemoimmunotherapy. Ingenol-3-angelate (I3A), an emerging antitumor drug with dual chemotherapeutic and immune response-eliciting effects, is expected to exert synergistic effects when administered in combination with DOX. I3A induces the ICD of PCa cells by triggering mitophagy and apoptosis and promotes the normalization of tumor vessels, resulting in sufficient infiltration of immune cells into tumors. A synergistic effect of I3A and DOX was observed in vitro at a molar ratio of 1:4. To codeliver this ratio of I3A and DOX to tumor and ensure their uptake, we designed a dual-targeting delivery system, polylactide-poly(ethylene) glycol-2-(3-((S)-5-amino-1-carboxypentyl)-ureido) pentanedioate/triphenylphosphonium (PLA-PEG-ACUPA/TPP), which targets prostate-specific membrane antigen (PSMA) and mitochondria. Delivery of these nanomedicines led to inhibited tumor growth and a strong antitumor immune response. This study sheds light on the mitophagic and antiangiogenic mechanisms underlying I3A treatment of PCa and provides a strategy for combining vascular normalization and chemoimmunotherapy for PCa treatment.

1. Introduction

Among the various types of cancer, prostate cancer (PCa) is thought to have the highest new incidence rate in males in recent years, and PCa is one of the primary causes of cancer-related death in males worldwide [1]. Although some patients with localized PCa can benefit from surgery or radiation therapy, relapse and metastasis occur in many patients [2]. Androgen deprivation therapy (ADT) is currently a standard treatment for prostate cancer; however, most patients eventually become resistant to this therapy during the course of treatment, leading to the expansion and spread of the cancer and resulting in a condition termed metastatic castration-resistant prostate cancer (mCRPC) [3]. Chemotherapeutic agents that have been approved for mCRPC treatment also cause severe resistance upon treatment initiation, leading to only moderately prolonged survival in the clinic [4].

Prostate cancer is characterized by a "cold" immunological tumor microenvironment with poor immune cell infiltration and low immunogenicity, and this microenvironment results in a markedly decreased response rate to immune checkpoint blockade therapy in prostate cancer patients [5,6]. Active immune escape protects PCa cells from surveillance

* Corresponding author. Key Laboratory of Marine Drugs, Chinese Ministry of Education, School of Medicine and Pharmacy, Ocean University of China, Qingdao, 266003, PR China.
** Corresponding author.
E-mail addresses: Wangsurgeon2000@163.com (P. Wang), cheng13980029671@163.com (C. Wang).
[1] These authors contributed equally to this work.

https://doi.org/10.1016/j.mtbio.2021.100189
Received 24 October 2021; Received in revised form 9 December 2021; Accepted 11 December 2021
Available online 13 December 2021

and destruction by the immune system, but immunogenic cell death (ICD), a specific form of apoptosis, allows immunocompetent hosts to mount specific immune responses against antigens derived from dying cells through immune-dependent mechanisms [7]. The mechanism by which cells undergo ICD is characterized by concomitant changes in immunogenic damage-associated molecular patterns (DAMPs), including the preapoptotic exposure of the endoplasmic reticulum-produced chaperone calreticulin (CRT) on the cell surface, the postapoptotic release of high mobility group box 1 (HMGB1), and the autophagy-driven release of ATP during the membrane blebbing phase of apoptosis [8]. DAMPs are a class of natural endogenous adjuvants that are typically hidden within living cells and stimulate the adaptive immune system in response to danger signals. Exposure of the CRT "eat me" signal on the cell membrane promotes the phagocytosis of dying tumor cells and the subsequent presentation of tumor-associated antigens by dendritic cells (DCs), generating an immune response [9]. End-stage tumor cells release ATP (a "find me" signal), which enables the recruitment of DCs and facilitates cytotoxic T lymphocyte (CTL) infiltration into tumors [10]. The release of HMGB1 into the extracellular compartment as a danger signal can stimulate DCs maturation and antigen presentation to CTLs upon binding to Toll-like receptor 4 (TLR4) on DCs and triggering the MyD88 signaling pathway [11]. In general, these DAMPs can directly integrate and activate DCs, which subsequently attract T cells into the tumor bed and exert immunological effects [7,12,13]. This endogenous antineoplastic immune response might be an effective strategy to reduce tumor-related mortality. The anthracycline chemotherapeutic agent doxorubicin (DOX) not only contributes to neoplastic cell death but also enhances antitumor immunity by causing the immunogenic demise of cancer cells [14,15]. Although DOX is a representative chemotherapeutic agent, the DOX-induced immunogenic death of tumor cells has not received enough attention because DOX is relatively inefficient in robustly promoting ICD due to a variety of restrictive circumstances and DOX treatment tends to frequently result in tumor relapse [16–18]. Further investigation is urgently required to identify drugs with immunogenic potential that can be administered either alone or in combination.

Autophagy is a process of self-degradation in which cells specifically eliminate damaged or unneeded components, including organelles and proteins, by sequestering them in double-membrane phagophores that form autophagosomes and subsequently fuse with lysosomes to form autophagolysosomes, which degrade the captured cellular contents [19,20]. In the context of chemotherapy-induced ICD, autophagy was reported to potentiate ATP release and induce antitumor immune responses, and it can attract DCs that express purinergic receptors [21]. Mitophagy, a type of selective autophagy, exerts extracellular homeostatic effects and is instrumental in ATP release, which is a pivotal signal for tumor cell activation in response to immunogenic chemotherapy [21–23]. Autophagy is required for the release of ATP from cells undergoing immunogenic death; thus, autophagy activators can augment the immune response activated by ICD inducers. To this end, further activation of autophagy may be an efficacious approach to enhance ICD-induced immune responses.

Ingenol-3-angelate (I3A), which is extracted from the sap of the *Euphorbia peplus* plant, is a natural diterpene ester that acts as a unique small-molecule drug that can be combined with chemotherapy (for a proapoptotic effect) and immunotherapy (for an immunostimulatory effect). It was reported that I3A promotes T-cell proliferation and survival through the PKC signaling pathway, induces tumor cell apoptosis through mitochondrial swelling, causes tumor vascular structure disruption and has adjuvant properties, such as upregulating Th1 cytokine expression and increasing CD80 and CD86 levels on DCs, resulting in the remarkable expansion of $CD4^+$ and $CD8^+$ T cells in neoplasms [24–27]. Additionally, our previous experimental evidence indicated that I3A induces the immunogenic death of tumor cells [28]; however, the underlying mechanism remains unclear. Therefore, we hypothesized that I3A-activated autophagy may enhance DOX-induced ICD and that the coadministration of both I3A and DOX can induce a potent host immune response that leads to synergistic effects.

However, vascular abnormalities attributed to VEGF contribute to tumor immune evasion in most patients with solid tumors [29]. High interstitial fluid pressure (IFP) and hypoperfusion caused by tumor vascular dysfunction prevent cytotoxic drugs and ICD-activated immune effector cells from entering the blood circulation and reaching tumors, thereby limiting their anticancer activity [30]. In fact, the results of several preclinical studies demonstrated the effectiveness of antiangiogenic agents administered in conjunction with other immunotherapies [29]. In addition, our findings demonstrated that I3A can inhibit VEGF production, exert antiangiogenic effects, and promote tumor vasculature normalization, thus enabling the deep penetration of drugs and adequate infiltration of ICD-activated immune cells into tumors.

Herein, we prove that I3A not only induces mitophagy and apoptosis, which are followed by activation of ICD in tumor cells but also inhibits VEGF signaling pathway activation, thereby promoting vascular normalization. Notably, the combination of I3A and DOX exerted substantial synergistic effects and exhibited antitumor properties at a lower dose than either I3A or DOX alone. However, the hydrophobicity, poor stability and off-target toxicity of this drug combination restrict its application in vivo; therefore, we constructed a sequential targeting delivery system consisting of polylactide (PLA)-polyethylene glycol (PEG)-2-(3-((S)-5-amino-1-carboxypentyl)-ureido) pentanedioate (ACUPA, targeting PMSA)/triphenylphosphonium (TPP, targeting mitochondria) nanoparticle formulations (NPs) to coencapsulate I3A and DOX (Scheme 1). In vivo and in vitro experiments with these nanoparticles demonstrated that I3A/DOX NPs-ACUPA/TPP (I3A/DOX NP-A/T) can be effectively delivered to tumor sites, release drugs in the appropriate ratio, promote vascular normalization, elicit antineoplastic immunity, and promote the accumulation of drugs and immune cells inside tumors. Preclinical evidence suggests a link between I3A and ICD, provides an effective immune-based cancer treatment strategy, and reveals future directions for research and clinical trials.

2. Materials and methods

2.1. Materials and reagents

Doxorubicin-free base (DOX) and I3A were purchased from Amgicam (Shanghai, China) and Nanjing DASF Corporation (Nanjing, China), respectively. Roswell Park Memorial Institute (RPMI) 1640 medium,

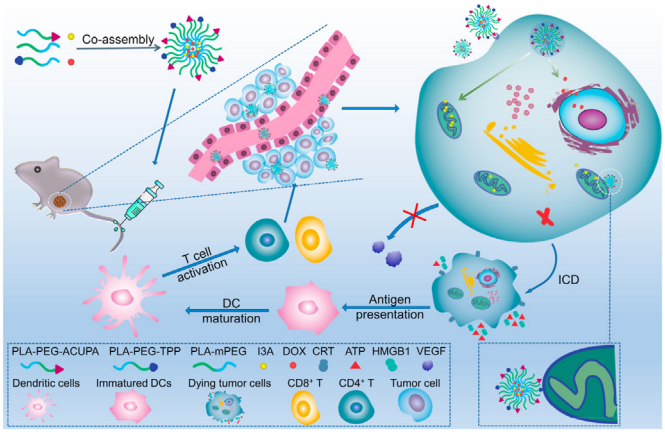

Scheme 1. Schematic representation of the dual-targeting delivery system for the codelivery of I3A and DOX for chemoimmunotherapy. After the tail vein injection of the nanomedicine, I3A/DOX NP-A/T delivers the drugs to the cytoplasm and mitochondria through cascade targeting, which induces ICD and inhibits VEGF production in tumor cells. DAMPs are released from dying tumor cells to promote dendritic cell maturation and antigen presentation, and subsequently activate T cells to kill tumor cells.

fetal bovine serum (FBS) and trypsin-EDTA (0.25%) were purchased from Gibco (Thermo Fisher Scientific, Shanghai, China). MitoTracker Deep Red FM, 1,1′-dioctadecyl-3,3,3′,3′-tetramethylindotricarbocyanine iodide (DiR) and 3,3′-dioctadecyloxacarbocyanine perchlorate (DiO) were purchased from Invitrogen (Thermo Fisher Scientific, Shanghai, China). Methoxy-terminated PEG-poly(D,L-lactide) ($mPEG_{2000}$-PLA_{2000}), amino-terminated PEG_{2000}-PLA_{2000} (NH_2-PEG_{2000}-PLA_{2000}) and carboxyl-terminated PEG_{2000}-PLA_{2000} (HOOC-PEG_{2000}-PLA_{2000}) were synthesized by Xi'an Ruixi Biological Technology Corporation (Shanxi, China). A dead cell apoptosis kit with Annexin V-fluorescein isothiocyanate (FITC)/propidium iodide (PI), a cell counting kit-8 (CCK-8), an ATP assay kit and a bicinchoninic acid (BCA) protein assay kit were obtained from Elabscience Biotechnology Corporation (Wuhan, China). ELISA kits, including interferon-γ (IFN-γ), tumor necrosis factor-alpha (TNF-α), and interleukin-12 (IL-12) ELISA kits, were purchased from Solarbio Corporation (Beijing, China). A fluorescent terminal deoxynucleotidyl transferase dTUP nick labeling (TUNEL) staining kit was obtained from Promega (Beijing, China). 1-(3-Dimethylaminopropyl)-3-ethylcarbodiimide hydrochloride (EDC), 4-dimethylaminopyridine (DMAP) and N-hydroxysuccinimide (NHS) were purchased from Sigma Aldrich (Shanghai, China). All the other reagents and chemicals were of analytical grade or higher purity.

2.2. Animals

C57BL/6 mice (6-week-old males) and BALB/C nude mice (6-week-old males) were purchased from Charles River Laboratories (Beijing, China) and maintained under the appropriate conditions. The animals were housed in a pathogen-free and thermoregulated environment with a 12-h light/dark cycle and were given access to food and water ad libitum. All the experimental protocols were approved by and conducted in accordance with the Ethics Committee of Experimental Animal Care, Ocean University of China.

2.3. Antibodies

The antibodies used in the flow cytometry, western blotting and immunofluorescence experiments are listed in Table S1.

2.4. CCK-8 assay

Cell viability was determined by CCK-8 assay after drug administration for 48 h. Approximately 5000 cells in 100 μL of medium were seeded in each well of a 96-well plate (JET), incubated for 24 h, and then treated with different drugs. After treatment, 10 μL of CCK-8 solution was added to each well and incubated for 4 h. Then we measured absorbance with a Multiskan FC microplate photometer (Thermo Fisher Scientific).

2.5. Colony formation assays

Cells were seeded in 6-well plates (5000 cells per well), incubated with various doses of drugs and maintained in an appropriate atmosphere for 2 weeks. These cells were subsequently fixed with 4% paraformaldehyde for 5 min and stained with 1% crystal violet, and then, the colonies were counted.

2.6. TUNEL assay

We labeled fragmented DNA with a TUNEL apoptosis detection kit (Promega). Drug-treated cells were fixed with 4% paraformaldehyde and subsequently rinsed with phosphate-buffered saline (PBS). After the fragmentation of genomic DNA, terminal deoxynucleotidyl transferase (TdT) catalyzes the addition of a green fluorescent probe (fluorescein (FITC)-labeled dUTP) to exposed 3′-OH, and then the nuclei are with DAPI prior to detection by confocal laser scanning microscopy (CLSM; Leica TCS SP8 STED). The percentage of cells undergoing apoptosis, as indicated by TUNEL-positive nuclei, was determined with ImageJ software.

2.7. Flow cytometry analysis

The proportion of apoptotic cells after drug treatment was measured with an Annexin V-FITC/PI apoptosis detection kit. The experiment was performed according to the manufacturer's instructions. A mitochondrial fluorescent probe was applied to measure changes in the mitochondrial mass of live cells during I3A treatment; mitochondrial uptake of this probe was not dependent on membrane potential. Cells treated with I3A were seeded in 6-well plates and subsequently incubated with MitoTracker Deep Red FM for 30 min and then collected. The intracellular fluorescence intensity was detected by fluorescence-activated cell sorting (FACS) with a flow cytometer (Becton Dickinson LSR).

After treatment, tumor tissues were dissociated with a gentleMACS Dissociator (Miltenyi Biotec). The obtained single-cell suspensions were resuspended in cell staining buffer (BioLegend) and then incubated with fluorescent-conjugated antibodies (Table S1). Proportions of mature DCs, $CD4^+$ T cells and $CD8^+$ T cells were examined by FACS with flow cytometry (Becton Dickinson LSR). The experimental data were analyzed by FlowJo software.

2.8. Immunofluorescence

Cells were cultured in glass-bottom dishes, and after reaching the appropriate confluence, the cells were treated with different drugs. To detect changes in mitochondrial morphology, we incubated cells with the fluorescent probe MitoTracker Deep Red FM (100 nM) at 37 °C for 30 min in the dark. Before observing and photographing the cells directly with CLSM, the cells were shaken and washed three times with PBS in a shaker. To examine the colocalization of autophagosomes with mitochondria, the samples were fixed with 4% paraformaldehyde for 15 min followed by rinsing with PBS. The samples were then blocked with blocking buffer (5% normal goat serum and 0.3% Triton X-100 in PBS) for 1 h. The cells were incubated with primary antibody (diluted in 1% bovine serum albumin (BSA) and 0.3% Triton X-100 in PBS) in a humidified ambient atmosphere overnight at 4 °C. After washing with PBS, the cells were incubated with goat anti-rabbit IgG secondary antibody (AF488 conjugated, Sangon Biotech) for 1 h at room temperature in the dark. The nuclei were counterstained with ProLong Gold Antifade Mountant with DAPI (Thermo Fisher Scientific). CRT exposure on the cell surface and HMGB1 release were detected as described above. For the immunofluorescence staining of tissue slides, paraffin-embedded tumor tissue excised from mice was sectioned into slices and subsequently fixed, permeabilized, blocked and stained with antibodies overnight at 4 °C. The cell nuclei were stained with DAPI (Thermo Fisher Scientific) and then, the sections were observed using CLSM. The antibodies used for this experiment are listed in Table S1.

2.9. Western blotting

For western blotting, tumor cells were seeded in 6-well plates and treated with different drugs. After 24 h of incubation, the cells were washed three times with PBS and lysed with RIPA lysis buffer following a previously described protocol. Then, the protein concentration of the lysate was determined with a BCA protein assay kit. The collected protein samples were added to 10% SDS-PAGE protein loading buffer, electrophoresed and transferred to 0.45-μm PVDF membranes. Then, the membranes were slowly shaken on a shaker, blocked with 5% nonfat milk for 1 h at ambient temperature, and incubated with diluted primary antibodies overnight at 4 °C. Horseradish peroxidase (HRP)-labeled secondary antibodies (Multisciences) were incubated with the membranes for 2 h at room temperature, after which the antibody-labeled proteins on the membranes were detected and visualized.

2.10. ATP release assay

ATP levels released from cells treated with different agents were measured with an ATP assay kit. The tumor cells were seeded in 6-well plates and incubated for the optimum time with 200 μL of lysis buffer. After complete lysis, the cells were centrifuged at 12,000 g (Beckman Coulter L-100 XP) for 5 min at 4 °C, and the supernatants were removed for subsequent assay. The amount of luciferin catalyzed by ATP-dependent luciferase was measured with a Multiskan™ FC microplate photometer (Thermo Fisher Scientific).

2.11. Collaborative effect assessment

The free-drug combination index (CI) of DOX and I3A at different molar ratios was determined with CompuSyn software on the basis of the Chou and Talalay method [31]. CI values less than 0.1 were considered to indicate very strong synergism, values between 0.1 and 0.3 were considered to indicate strong synergism, and those between 0.3 and 0.7 were considered to indicate synergism.

2.12. Synthesis and characterization of ACUPA-Conjugated and TPP-Conjugated polymers

The targeting copolymers PLA-PEG-ACUPA and PLA-PEG-TPP were synthesized as previously reported [28]. PLA-PEG-COOH (0.5 mmol) was dissolved in chloroform, ACUPA (0.55 mmol) and NHS (1.0 mmol) were added to the reaction solution, and the reaction was stirred for 24 h at room temperature. After the reaction, 50% trifluoroacetic acid (TFA) was added and stirred for another 24 h to remove the protecting group, tert-butoxycarbonyl, from ACUPA. Then, the product was dried under a vacuum to remove the solvent, and the solid product obtained was dissolved in distilled H_2O (dH_2O) and purified by Amicon Ultra-15 (MW3000, Millipore). Purified PLA-PEG-ACUPA block copolymer was redissolved in dH_2O and lyophilized into powder.

The method for synthesizing PLA-PEG-TPP was similar to that described above for PLA-PEG-ACUPA. Briefly, TPP (0.3 mmol) and PLA-PEG-NH_2 (0.25 mmol) were dissolved in chloroform, and then, EDC (0.5 mmol) and DMAP (0.025 mmol) were added and stirred at room temperature for 30 min. After vacuum drying, the resulting PLA-PEG-TPP combination was dissolved in dH_2O and purified by ultrafiltration. The product was redissolved in dH_2O and then lyophilized for further use.

2.13. Preparation and characterization of ACUPA-Targeting and TPP-Targeting NPs with loaded drugs

Drug-loaded ACUPA NPs (NP-A) or ACUPA/TPP NPs (NP-A/T) were prepared by the nanoprecipitation method as previously reported. Briefly, 2 mg of I3A and 10 mg of DOX were dissolved in 2 mL of dimethyl sulfoxide (DMSO), and then, 93.05 mg of PLA-mPEG and 2.45 mg of PLA-PEG-ACUPA were mixed into the solution. The mixture was added dropwise to deionized water with agitation and stirred for 2 h to form nanoparticles. Drug-loaded nanoparticles were purified by ultrafiltration at 4000 g. The product was redissolved in dH_2O and then lyophilized for further use.

Drug-loaded NP-A/T was prepared as described above by codissolving 88.05 mg of PLA-mPEG, 5.0 mg of PLA-PEG-TPP, 2.45 mg of PLA-PEG-ACUPA in copolymer form, 2 mg of I3A and 10 mg of DOX in 2 mL of DMSO, and the subsequent steps were the same as those used to generate NP-A.

The NPs size and zeta potential were determined by a ZetaSizer Nano ZS90 (Malvern Panalytical). Morphological characterization of the NPs was determined by transmission electron microscopy (TEM; Thermo Fisher Scientific). Five microliters of NPs solution were added dropwise to a hydrophilized copper mesh, which was stained with uranyl acetate (added dropwise) for more than 1 min before imaging by TEM. Drug loading (DL) and encapsulation efficiency (EE) were calculated with the following equations: (encapsulated drug/weight of nanoparticles) × 100% and (encapsulated drug/addition of drug) × 100%. DL and EE were investigated using HPLC via an approach identical to that described in our previous report [27].

2.14. Cellular uptake and subcellular localization

RM-1 cells were seeded in a 6-well culture plate at a density of 1.0×10^5 cells/well. After being cultured for 24 h, the cells were incubated with different drugs (free DOX, I3A/DOX NP, I3A/DOX NP-A and I3A/DOX NP-A/T) at the same DOX concentration, 500 ng/mL, for 4 h at 37 °C. The fluorescence signals indicating cellular uptake were quantified by FACS, and 10,000 events were analyzed. To determine the subcellular localization of NP-A/T, RM-1 cells were cultured on coverslips in 6-well plates at 10^5 per well for 24 h at 37 °C. Then, the cells were incubated with DiO-labeled NP-A/T for 1 h and 4 h. After staining with MitoTracker Deep Red FM and washing with PBS, the coverslips were fixed using 4% paraformaldehyde. Finally, the coverslips were mounted with ProLong Gold Antifade Mountant with DAPI, and CLSM was performed.

2.15. Biodistribution

Lipophilic carbocyanine DiR was encapsulated in NPs to prepare DiR-labeled NP, NP-A or NP-A/T. The same dose of 2.5 mg/kg DiR was injected into the tail vein of BALB/C nude mice. At 4 h, 8 h, 12 h, and 24 h after DiR treatment, the mice were sacrificed, and ex vivo fluorescence images of the heart, liver, spleen, lung and kidney were obtained with the IVIS system (Caliper Life Sciences). The fluorescence intensity of each tissue was quantified. Then, tumor slices fixed with paraformaldehyde and stained with Hoechst 33,258 were observed under a fluorescence microscope.

2.16. Antitumor efficacy

RM-1 cell-derived xenograft (CDX) prostatic tumor models were established in C57BL/6 mice (weighing approximately 20 g). RM-1 cells were collected in the logarithmic phase of growth, and 1.0×10^6 cells were intravenously injected into the armpits of the mice. C57BL/6 mice with a tumor volume of approximately 100 mm^3 were randomly assigned into 5 groups (n = 12). Prostatic tumor-bearing mice were intravenously injected with PBS, I3A-loaded ACUPA NPs (I3A NP-A), DOX-loaded ACUPA NPs (DOX NP-A), I3A/DOX-loaded ACUPA NPs (I3A/DOX NP-A) or I3A/DOX-loaded ACUPA/TPP NPs (I3A/DOX NP-A/T) every 3 days for a total of 6 injections. Within this time period, tumor volume and body weight were recorded every other day. On the 18th day posttreatment, six mice from each group were euthanized for antitumor analysis, and the remaining mice (n = 6) were observed for survival analysis.

2.17. Cytokine examination

Tumor tissue samples were prepared according to the method described above. The levels of the cytokines IFN-γ, TNF-α and IL-12 in tumors were estimated with a mouse IFN-γ ELISA kit, mouse TNF-α ELISA kit and mouse IL-12 ELISA kit, respectively, following the manufacturer's protocols.

2.18. Immunohistochemistry and H&E staining

All the tissues were fixed overnight in 4% paraformaldehyde solution, dehydrated with sucrose solutions and embedded in paraffin, and then, the samples were cut into 4 μm thick sections for further staining. To determine the expression level of CD31, an immunohistochemistry assay was performed. Tumor tissue sections were fixed, permeabilized, blocked and subsequently stained with primary antibody overnight at 4 °C. After washing with PBS, the sections were incubated with biotin-labeled secondary antibody for 1 h at room temperature in the dark, incubated with

diaminobenzidine (DAB) and counterstained with hematoxylin. For a safety evaluation, tissue sections of organs (brains, hearts, livers, spleens, lungs and kidneys) were stained with H&E and then visualized with an optical microscope.

2.19. Statistical analysis

The data are presented as the mean ± standard deviation (mean ± SD) after analysis with GraphPad 8.0 software. The experiments were carried out in triplicate. To analyze differences between two groups, Student's *t*-test was performed, and to analyze differences among multiple groups, one-way analysis of variance (ANOVA) was performed. $*p < 0.05$, $**p < 0.01$, $***p < 0.001$, and $****p < 0.0001$ indicated significance, and significant differences were found between groups ($*p <$ 0.05).

3. Results and discussion

3.1. I3A inhibits PCa cell proliferation by enhancing apoptosis

To evaluate the tumor cell suppressive effect of I3A, a CCK-8 assay was first performed to evaluate the viability of the mouse RM-1 and human LNCaP cell lines after drug administration. After incubation of the cells with I3A for 48 h, the results showed a dose-dependent decrease in the viability of both I3A-treated RM-1 cells and LNCaP cells, with half maximal inhibitory concentration (IC50) values of 74.3 μM and 80.1 μM, respectively (Fig. 1A). Hence, remarkable PCa cell death occurred after drug treatment. As indicated in Fig. 1B and C, the colony formation assay

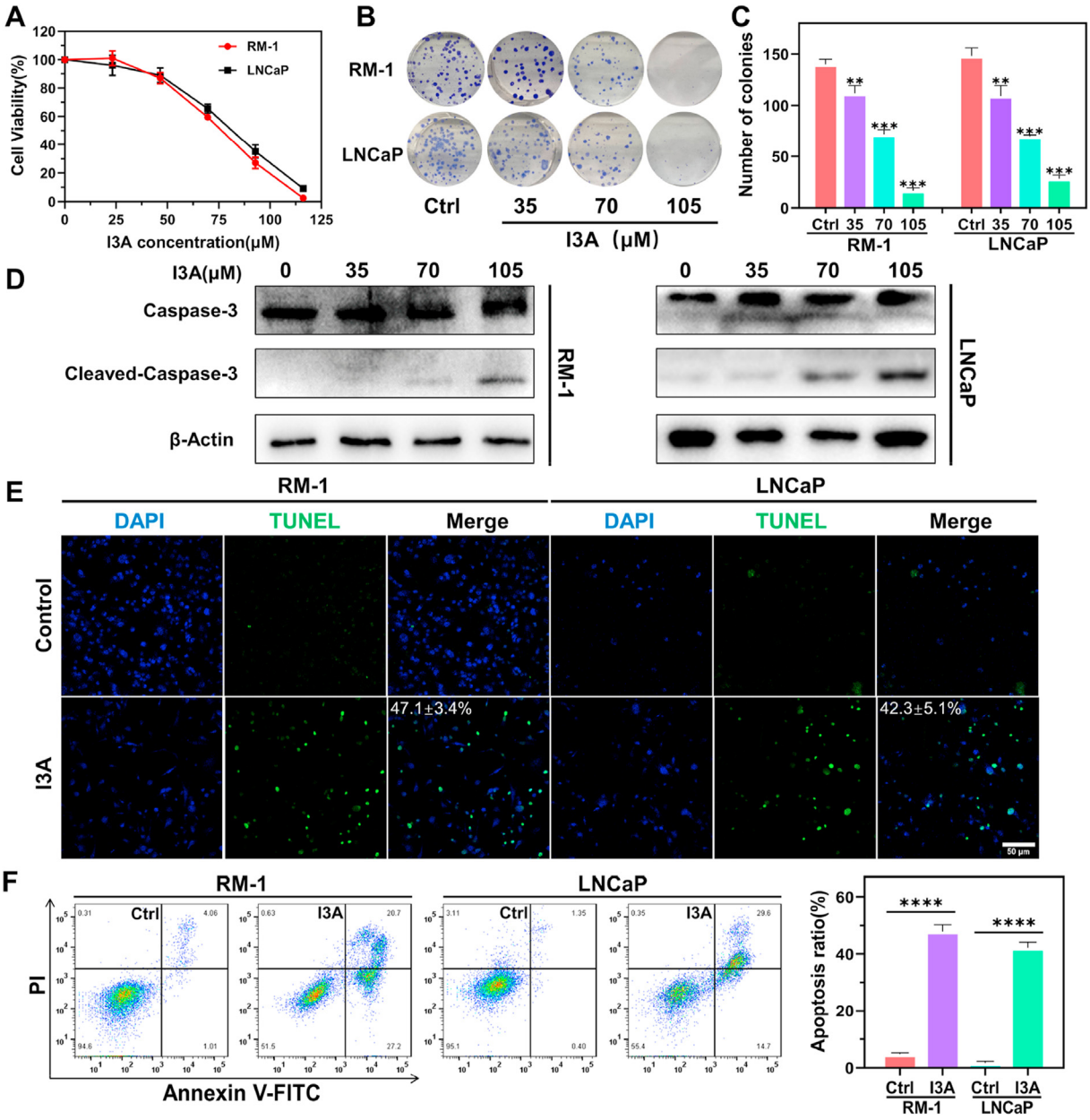

Fig. 1. I3A inhibits PCa cell proliferation and malignant transformation in vitro. (A) Inhibited proliferation of RM-1 and LNCaP PCa cells treated with I3A at different concentrations (n = 3). (B) Colony formation of RM-1 and LNCaP cells treated with I3A. (C) Statistical analysis the experimental results shown in (B) (n = 3). (D) Western blotting of Caspase-3 and Cleaved-Caspase-3 protein levels after I3A treatment. (E) TUNEL assay of cell apoptosis after treatment with I3A, as determined by CLSM (blue, DAPI; green, TUNEL; scale bar, 50 μm). (F) FACS analysis of apoptotic cell proportions after treatment with I3A. The data are presented as the mean ± SD, $**p < 0.01$, $***p < 0.001$, $****p < 0.0001$.

demonstrated that the numbers of colonies in the drug-treated groups were decreased compared with that in the control group, and this effect increased with increasing drug concentration. To identify the contribution of I3A cytotoxicity to apoptosis induction in cancer cells, the levels of the apoptosis protein cleaved-caspase-3 were measured by western blotting (Fig. 1D). The results revealed a significant dose-dependent increase in the expression of this apoptotic protein in PCa cells after I3A treatment. Moreover, the TUNEL assay showed that apoptotic signals induced by I3A were associated with inhibited tumor cell proliferation (Fig. 1E). An identical effect was obtained with the Annexin V-FITC/PI flow cytometry assay (Fig. 1F).

3.2. I3A enhances mitophagy, inhibits VEGF expression, and induces ICD in PCa cells

Autophagy is conducive to immunogenic death and activates the innate immune system, which eliminates dying tumor cells [19]. To evaluate whether I3A can induce autophagy in PCa cells, western blotting analysis of autophagy marker expression was performed, and I3A was found to promote the conversion of cytoplasmic LC3-I to lipidated LC3-II while downregulating the expression of p62, suggesting that I3A can trigger autophagy (Fig. 2A and S1). Moreover, western blotting indicated that I3A inhibited the expression of the angiogenesis-stimulating factor VEGF. To verify that I3A treatment damages to mitochondria in tumor cells, the morphology of mitochondria was observed by CLSM (Fig. 2B, i). Compared to the normal mitochondria in the control group, the mitochondria in the group subjected to I3A treatment were swollen and lost the linear morphology observed after treatment. In the I3A-treated group, mitochondria also displayed swelling and lack of cristae, and a decrease in the number of normal mitochondria was observed (Fig. 2B, ii). In addition, the mitochondrial mass of tumor cells after I3A treatment was quantified by flow cytometry, and the results showed that the fluorescence intensity of mitochondria labeled with the mitochondrial dye MitoTracker Deep Red FM was significantly reduced following drug

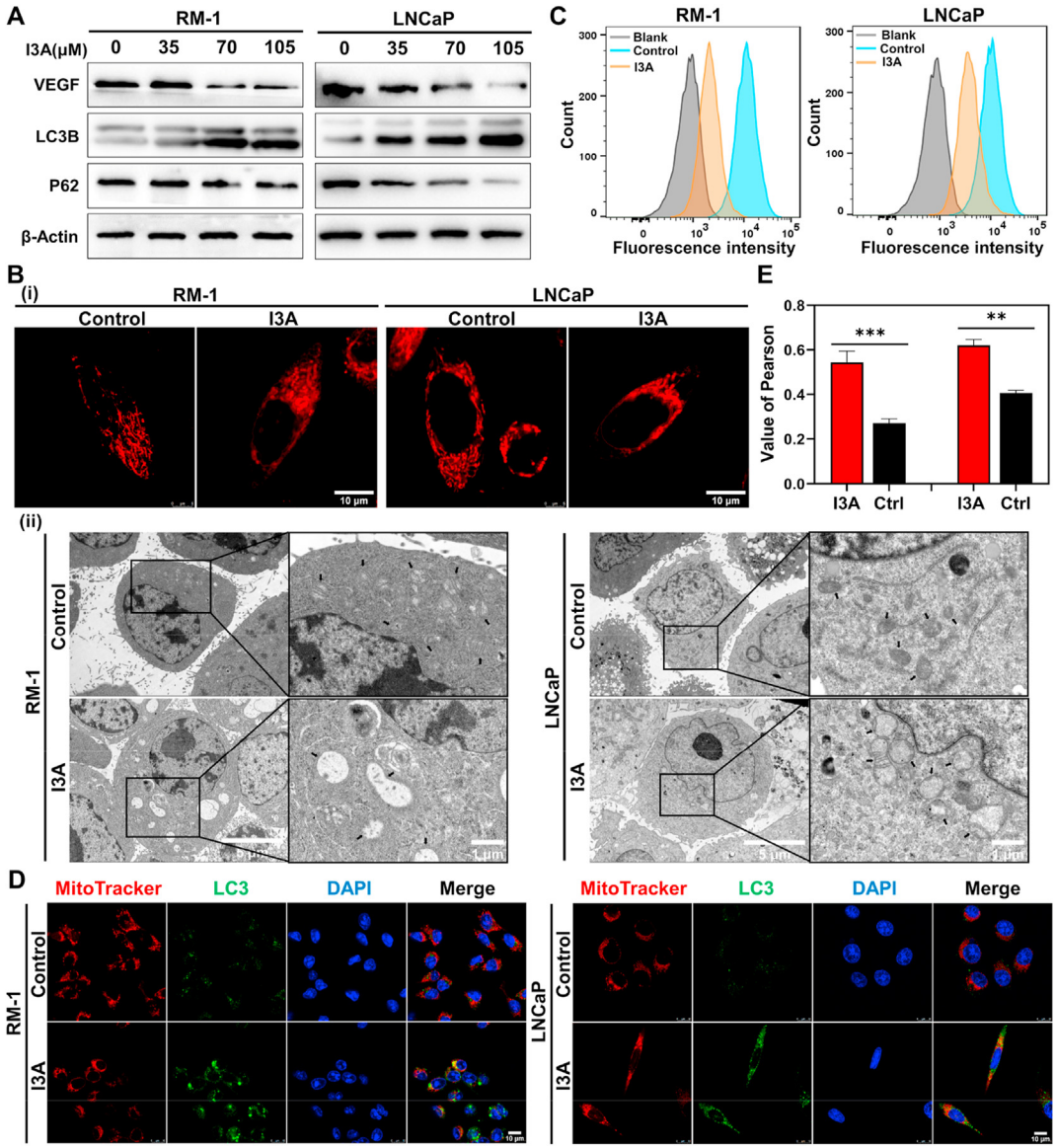

Fig. 2. I3A inhibits VEGF production and induces mitophagy in PCa cells. (A) Western blotting of VEGF, LC3 and p62 expression in PCa cells after treatment with the indicated concentration of I3A for 24 h. (B) Mitochondrial morphology of RM-1 and LNCaP cells treated with 70 μM I3A as observed by CLSM (i; red, mitochondria; scale bar, 10 μm) and TEM (ii; black arrow, mitochondria; scale bar, 5 μm and 1 μm). (C) Mitochondrial mass determined by FACS after cell staining with MitoTracker Deep Red FM. (D) Immunostaining of mitochondria and LC3 (autophagy marker) to determine mitophagy occurrence after treatment with 70 μM I3A (blue, DAPI; red, mitochondria; green, LC3; scale bar, 10 μm). (E) Pearson coefficient value of the data shown in (D). The data are presented as the mean ± SD, **p < 0.01, ***p < 0.001.

treatment, i.e., the mitochondrial mass was reduced (Fig. 2C). These results suggest that I3A is capable of interacting with mitochondria and contributing to mitochondrial depletion in cancer cells. To confirm that I3A-induced mitochondrial damage promoted autophagy, the formation of LC3-labeled autophagosomes and the degree of autophagosome colocalization with MitoTracker Deep Red FM-labeled mitochondria were analyzed by immunofluorescence. Interestingly, CLSM demonstrated that I3A obviously promoted autophagy, and the Pearson correlation coefficient of autophagosome and mitochondrial colocalization showed that I3A markedly increased their colocalization, as analyzed with ImageJ software (Fig. 2D and E). The hallmarks of the onset of ICD are CRT exposure, ATP secretion and HMGB1 release. Therefore, the effects of I3A on the levels of CRT, ATP and HMGB1 in both PCa cell lines were examined by fluorescence microscopy. Upon treatment of tumor cells with I3A for a period of time, the translocation of CRT from the endoplasmic reticulum to the cell membrane, the release of HMGB1 from the nucleus to the cytoplasm, and the release of ATP were observed, as illustrated in Figure S2. Thus, the ability of I3A not only to stimulate autophagy and suppress VEGF expression but also to induce subsequent ICD was high, indicating that I3A has great potential for use in immunotherapy.

3.3. I3A with DOX Co-induced ICD

Although DOX effectively suppresses most tumor cells, the resulting degree of ICD, which is a form of cell death, remains low [16–18]. For this reason, to maximize the ICD induced by DOX, the addition of I3A, which induces mitophagy, has been suggested to achieve a synergistic effect. A CCK-8 assay was performed 48 h posttreatment to determine the cytotoxic effects of different molar ratios of the I3A-DOX combination. Upon incubation with the drug combination at different molar ratios (I3A:DOX), including 1:1, 1:4, 1:8, 4:1, 8:1 and 15:1, the IC50 and CI values were measured (Fig. 3A). Notably, when the molar ratio of I3A:DOX was 1:4, the CI value was the lowest when the fraction affected (Fa) was equal to 0.5, representing the strongest synergistic effect observed in this experiment. Compared with free I3A and DOX, the I3A:DOX ratio of 1:4 (0.11 μM and 0.44 μM, respectively) had a reduced IC50 value. This ratio allows for higher therapeutic efficacy with lower doses and fewer side effects. Correspondingly, at certain concentrations (e.g., 0.11 μM I3A:0.44 μM DOX), the combination of I3A and DOX significantly inhibited the proliferation of cancer cells compared to the individual drugs, which was verified by colony formation assays and flow cytometry analysis of apoptosis (Fig. 3B–E). Subsequently, extracellular ATP levels were measured with an ATP assay kit according to the manufacturer's instructions, and the results showed that the combined drug group exhibited greater ATP release than the free drug groups (Fig. 3F). Moreover, CRT exposure and HMGB1 release were monitored by CLSM (Fig. 3G). The results revealed that a substantial number of CRT- and HMGB1-stained cells were detected in the combination group, while virtually no fluorescence was observed in the free drug groups, suggesting augmented ICD-associated immunogenicity in the combination group. In general, a low dose of the combination drug regimen exerted a synergistic effect and enhanced ICD in vitro.

3.4. Preparation and characterization of I3A/DOX-loaded NP-A/T

Although excellent results have been obtained in in vitro experiments with the combination of I3A and DOX, the potential use of this combination in vivo is extremely limited by strong hydrophobicity and acute toxicity. In addition, to ensure that these two drugs can accumulate in tumor sites at appropriate synergistic ratios, effectively circulate systemically, and achieve on-target delivery, a dual-delivery system was developed to coencapsulate I3A and DOX into PLA-PEG-ACUPA/TPP through nanoprecipitation (Fig. 4A). The morphological characterization of I3A/DOX NP-A/T performed with TEM showed micelle-like structures with a diameter of approximately 30 nm (Fig. 4B). Furthermore, dynamic light scattering analysis demonstrated that the dual-delivery system consisting of I3A/DOX NP-A/T had an average diameter of 30 nm, which was consistent with the TEM images (Fig. 4C). The zeta potential analysis revealed a potential of −30 mV for I3A/DOX NP-A/T (Fig. 4D). In addition, the stability of I3A/DOX NP-A/T was measured in vitro. The data from this in vitro experiment revealed that the size of the I3A/DOX NP-A/T did not change appreciably within 48 h when was incubated with PBS at pH 7.4 or 10% FBS-supplemented RPMI-

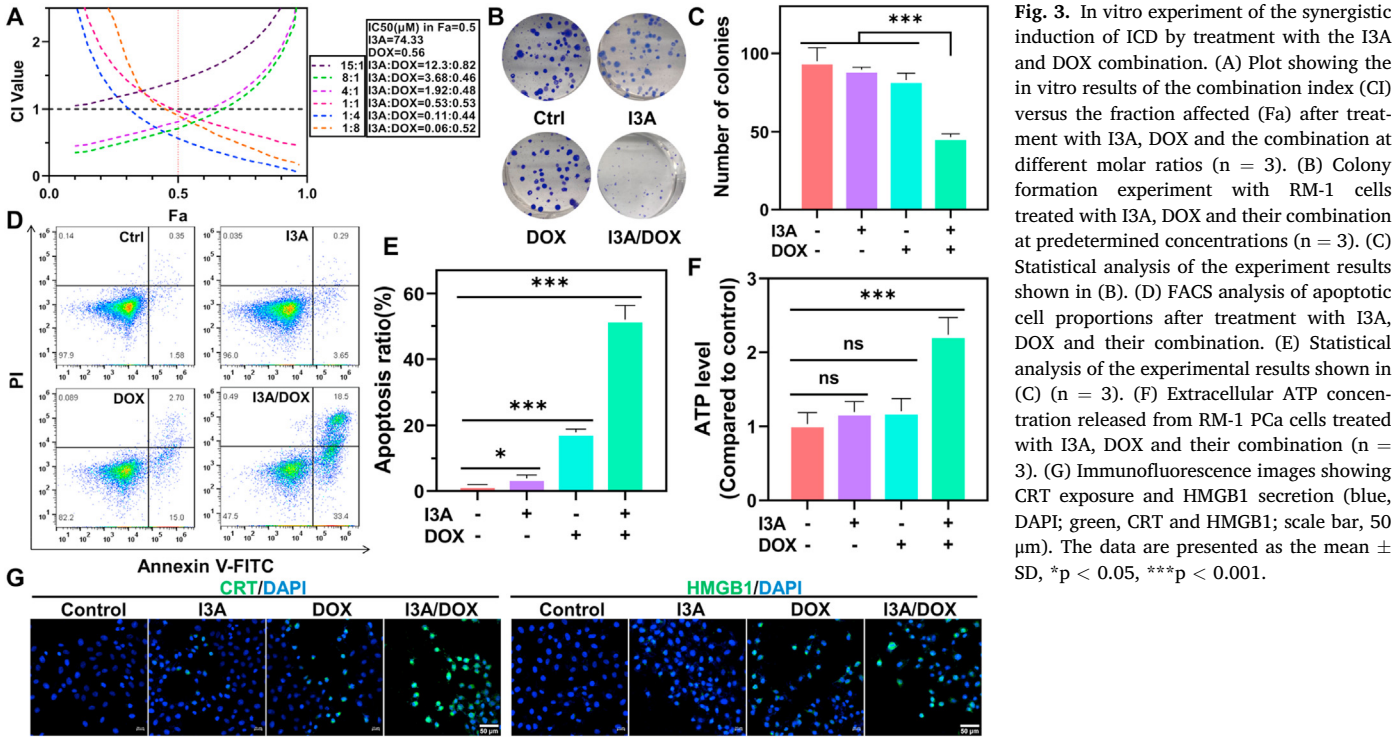

Fig. 3. In vitro experiment of the synergistic induction of ICD by treatment with the I3A and DOX combination. (A) Plot showing the in vitro results of the combination index (CI) versus the fraction affected (Fa) after treatment with I3A, DOX and the combination at different molar ratios (n = 3). (B) Colony formation experiment with RM-1 cells treated with I3A, DOX and their combination at predetermined concentrations (n = 3). (C) Statistical analysis of the experiment results shown in (B). (D) FACS analysis of apoptotic cell proportions after treatment with I3A, DOX and their combination. (E) Statistical analysis of the experimental results shown in (C) (n = 3). (F) Extracellular ATP concentration released from RM-1 PCa cells treated with I3A, DOX and their combination (n = 3). (G) Immunofluorescence images showing CRT exposure and HMGB1 secretion (blue, DAPI; green, CRT and HMGB1; scale bar, 50 μm). The data are presented as the mean ± SD, *p < 0.05, ***p < 0.001.

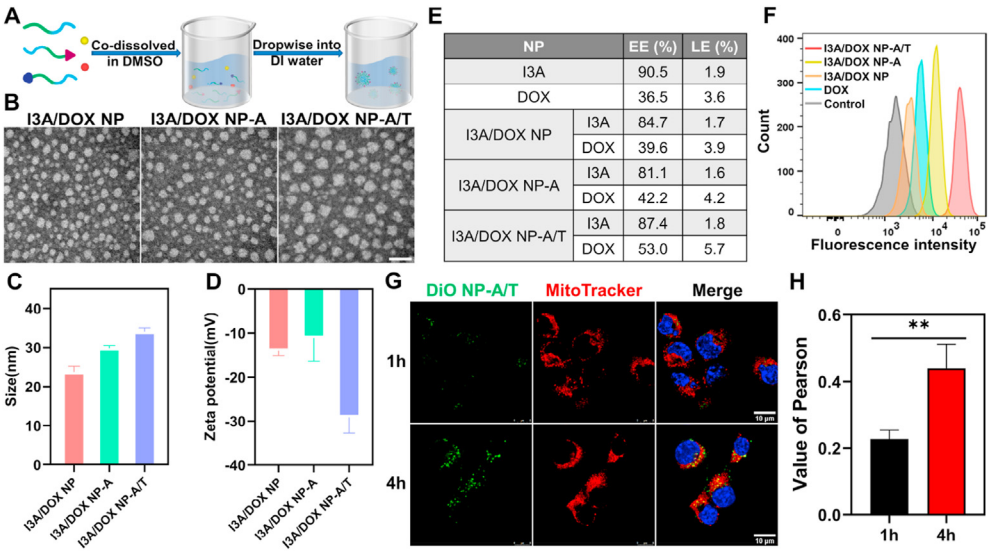

NP		EE (%)	LE (%)
I3A		90.5	1.9
DOX		36.5	3.6
I3A/DOX NP	I3A	84.7	1.7
	DOX	39.6	3.9
I3A/DOX NP-A	I3A	81.1	1.6
	DOX	42.2	4.2
I3A/DOX NP-A/T	I3A	87.4	1.8
	DOX	53.0	5.7

Fig. 4. Construction of the I3A and DOX sequentially targeted dual-delivery NPs system. (A) Schematic of coencapsulation of I3A and DOX into the NPs. (B) TEM images showing the morphology of the NPs (scale bar, 50 nm). (C) Particle size distribution of the NPs. (D) Zeta potential of the NPs. (E) EE and LC of I3A and DOX in the NPs. (F) Flow cytometric analysis of the cellular uptake of drugs after treatment with different DOX-loaded NPs. (G) Immunofluorescence images showing intracellular delivery of DiO-loaded NP-A/T into RM-1 cells at 1 h and 4 h, as observed by CLSM (blue, DAPI; green, DiO NP-A/T; red, mitochondria; scale bar, 10 μm). (H) Pearson coefficient value of the delivery shown in (G). The data are presented as the mean ± SD, $^{**}p < 0.01$.

1640 cell culture media, indicating superior stability (Figure S3). The encapsulation efficiency (EE) and loading efficiency (LE) of I3A and DOX were 90.5% and 36.5%, respectively (Fig. 4E). In experiments in which the loading ratio of I3A and DOX was changed, I3A and DOX were successfully loaded into the carrier at a molar ratio of 1:4, and the EE and LE were 84.7% and 1.8% and 53.0% and 5.7% for I3A and DOX, respectively (Fig. 4E).

Next, the release kinetics of the DOX and I3A drugs from I3A/DOX NP-A/T were further evaluated by simulating physiological conditions (pH 7.4, PBS) and acidic lysosomal/endosomal conditions (pH 5.5, PBS) (Figure S4). Approximately 40% of both drugs were released from the I3A/DOX NP-A/T at 4 h of incubation, and more than 90% of these drugs were released within 24 h. These data indicate that I3A/DOX NP-A/T were capable of releasing large amounts of these drugs in an efficacious manner following uptake by tumor cells. In contrast, at pH 7.4, I3A/DOX NP-A/T released only approximately 20% of both drugs at 24 h, indicating that the I3A/DOX NP-A/T were stable at normal physiological pH but released their cargo in the acidic environment of the lysosomes/endosomes.

3.5. Cellular uptake of nanoparticles in vitro

To induce ICD in tumor cells, efficient cellular uptake of ICD inducers by tumor cells is critical. ACUPA is a small-molecule inhibitor that targets prostate-specific membrane antigen (PSMA), a transmembrane glycoprotein capable of triggering receptor-mediated endocytosis that is overexpressed on the surface of PCa cells and in the neovasculature of many solid tumors [32,33]. TPP, a molecule with cationic properties and lipophilicity, can interact with mitochondria with a negative membrane potential, thus specifically allowing mitochondrial aggregation [34,35]. To evaluate the impacts of nanoparticles modified with the PSMA-targeting peptide ACUPA and mitochondria-targeting TPP on the cellular uptake of drugs, RM-1 cells were separately incubated with free DOX, I3A/DOX NP, I3A/DOX NP-A and I3A/DOX NP-A/T at the same DOX concentration for 4 h. Then drug internalization was monitored by flow cytometry. As shown in Fig. 4F, the intracellular level of DOX in the groups with a targeting carrier was higher than that in the free DOX group. In addition, the DOX NP-A/T group exhibited the highest intracellular DOX amount compared to the DOX NP-A group and DOX NP group, indicating accelerated dual-targeting drug delivery into tumor cells. Subsequently, the subcellular localization of NP-A/T was confirmed by CLSM (Fig. 4G). Tumor cells were incubated with NP-A/T loaded with DiO (green), a fluorescent dye, for 1 h and 4 h. Mitochondria were then labeled with MitoTracker Deep Red FM (red), and the Pearson correlation coefficient of mitochondrial and nanoparticle colocalization was calculated by ImageJ software (Fig. 4H). The results showed that with an extended incubation time, NP-A/T effectively targeted mitochondria. In addition, the cell viability assay showed that I3A/DOX NP-A/T exerted obvious cytotoxic effects on tumor cells (Figure S5).

3.6. Biodistribution and deep penetration in vivo

Considering the aforementioned in vitro cellular uptake, we verified the tumor-targeting ability of the nanoparticles in vivo using RM-1 tumor-bearing nude mice. DiR-labeled NP, NP-A and NP-A/T were injected into nude mice via the tail vein and visualized using an in vivo imaging IVIS system at the specified time points of 4 h, 8 h, 12 h and 24 h. Twenty-four hours after injection, DiR-labeled NP-A/T demonstrated a robust fluorescent response signal at the tumor site, which was higher than that of NP and NP-A, proving the remarkable tumor-targeting ability of NP-A/T (Figure S6A). Tumor-bearing nude mice were sacrificed 4 h, 8 h, 12 h and 24 h after NPs injection, and the entire tumor tissue and major organs (heart, liver, spleen, lung, and kidney) were excised for ex vivo imaging (Figure S6A). In accordance with the in vivo imaging results, the fluorescence intensity of NP-A/T in the tumor site was higher than that of the two other treatments and displayed a similar biodistribution (Figure S6B). Next, the excised tumor tissues were sectioned and stained with DAPI. In comparison with the other two groups, the NP-A/T group presented with higher red fluorescence intensity, demonstrating better bioaccumulation and bioconcentration at the tumor site, as observed by fluorescence microscopy (Figure S7). Even for tumor tissues with a dense stroma, the red fluorescence of DiR was detected inside the tumor, illustrating the enhanced and deep penetration capability of NP-A/T. According to these results, loading drugs into NP-A/T enabled tumor accumulation and deep penetration.

3.7. In vivo antitumor effects and immune-suppressive microenvironment remodeling induced by I3A/DOX NP-A/T

To evaluate the antineoplastic and immune activation effects of different formulations in vivo, a RM-1 tumor-bearing C57BL/6 mouse model was established. When tumor size reached 100 mm^3, C57BL/6 mice were randomly divided into five groups and injected with PBS, I3A NP-A (3 mg/kg I3A), DOX NP-A (5 mg/kg DOX), I3A/DOX NP-A (1 mg/kg I3A and 4 mg/kg DOX) or I3A/DOX NP-A/T (1 mg/kg I3A and 4 mg/kg DOX) via the tail vein every 3 days for 18 days (Fig. 5A). The tumor volumes of the mice were measured every 3 days after the initiation of treatment. The I3A NP-A, DOX NP-A, I3A/DOX NP-A and I3A/DOX NP-

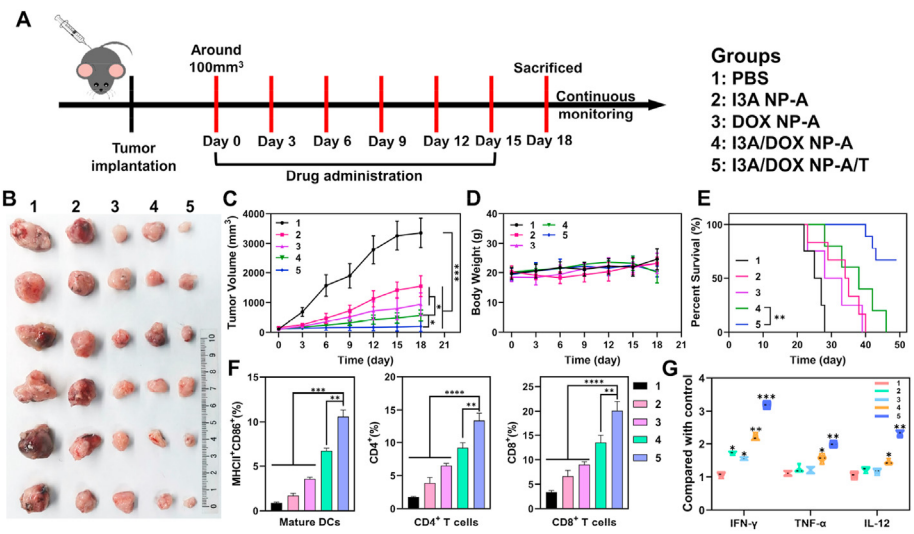

Fig. 5. In vivo tumor suppression and immune microenvironment remodeling caused by NPs. (A) Schematic illustration of tumor inoculation and timing of the treatment. (B) Ex vivo graphs showing the tumors 18 days after treatment with PBS, I3A NP-A, DOX NP-A, I3A/DOX NP-A or I3A/DOX NP-A/T. (C) Tumor volume, (D) body weight and (E) survival rate of tumor-bearing mice in various treatment groups (n = 6). (F) Flow cytometric analysis of the proportions of immune cells, including mature DCs, $CD4^+$ T cells and $CD8^+$ T cells, in tumors after exposure to different treatments (n = 3). (G) Expression of IFN-γ, TNF-α and IL-12 in tumors in different treatment groups (n = 6). The data are presented as the mean ± SD, *p < 0.05, **p < 0.01, ***p < 0.001, ****p < 0.0001.

A/T groups showed tumor growth suppressive effects compared to the control group (Fig. 5B and C). The results revealed that the optimal tumor suppression effect occurred in the I3A/DOX NP-A/T treatment group, which also had the longest lifespan (Fig. 5E). This was ascribed to the TPP-targeting head that enabled deep tumor penetration by I3A/DOX NP-A/T, as indicated by the results of the in vivo biodistribution experiment (Figure S6). Notably, there was no noticeable weight loss in any group throughout the study, indicating the reliable biosafety of the dual-delivery system (Fig. 5D). To further investigate the biocompatibility of these nanomedicines, major organs (heart, liver, spleen, lung and kidney) were sectioned and stained with H&E following a tumor suppression assay. Images were captured under a microscope and showed no obvious damage or toxicity in the major organs (Figure S8).

In the tumor microenvironment (TME), VGEF induces tumor-associated immunosuppression through multiple mechanisms, including direct inhibition of CTL transport, proliferation and effector functions, inhibition of DCs maturation and antigen presentation, inhibition of T cell activation, promotion of the recruitment and proliferation of immunosuppressive cells such as Treg cells, promotion of angiogenesis, and promotion of abnormalities in the tumor vascular system [29]. Therefore, vascular normalization is helpful for normalizing the abnormal tumor vascular system and increasing the infiltration of immune cells, thus improving the immunotherapeutic effect and eventually changing the immunosuppressive TME to an immune-enhancing TME. To further evaluate whether I3A/DOX NP-A/T promotes tumor vascular normalization, the expression of VEGF in tumor tissue was measured by CLSM. The expression of VEGF was negligible in the I3A/DOX NP-A/T-treated group, while the expression level of VEGF in the DOX NP-A group was higher than that in the I3A NP-A and I3A/DOX NP-A groups, indicating that I3A effectively inhibited the expression of VEGF (Figure S9). After confirming that I3A inhibited VEGF expression, the degree of vessel normalization was assessed by CLSM. CD31 is considered to be a marker of tumor vasculature [36], and a decreased CD31 expression level, which was clearly observed in the I3A/DOX NP-A/T-treated group, denotes a trend of tumor vasculature normalization (Figure S10).

To examine the capability of I3A/DOX NP-A/T of inducing ICD in vivo, the expression levels of the ICD markers CRT and HMGB1 in tumor tissue were measured by CLSM (Figure S11). In contrast to the other groups, in the I3A/DOX NP-A/T group, CRT exposure and HMGB1 release were observed, and these effects were attributed to vascular normalization and deep penetration. Achieving immune regulation is pivotal to the initiation of ICD, in which DCs play a substantial role by elevating the immune response and infiltration of intratumoral CTLs. Accordingly, the proportion of immune cells, including activated DCs, $CD8^+$ T cells and $CD4^+$ T cells, was increased with I3A/DOX NP-A/T treatment (Fig. 5F and S12). Then, the levels of immunostimulatory cytokines were measured, and increased IFN-γ, IL-12 and TNF-α levels were detected at the tumor sites in the I3A/DOX NP-A/T group (Fig. 5G). Taken together, the results show that the dual-targeting drug delivery system promotes vascular normalization, facilitates deep penetration of nanomedicines, exerts synergistic effects, and reshapes the immunosuppressive TME, thus potentiating antineoplastic efficiency.

4. Conclusion

In summary, our study showed that I3A triggered ICD in human and murine PCa cells by eliciting mitophagy and apoptosis and inhibited VEGF expression in tumor cells to normalize tumor vasculature. In addition, at a low combined dose, I3A and DOX exerted a synergistic effect on ICD. Dual-targeting PLA-PEG-ACUPA/TPP nanoparticles co-deliver I3A and DOX into tumors to promote drug accumulation and deep penetration at tumor sites, as well as to enhance ICD. The nanomedicine combination eventually reverses the immunosuppressive microenvironment, transforming cold tumors into hot tumors and eliciting effective innate and adaptive antitumor immune responses. This study shows the translational potential of combination therapy based on the clinical exploration and discovery of novel ICD inducers.

Author contribution

Zhicheng Wang: Conceptualization, Methodology, Formal analysis, Investigation, Visualization, Writing – original draft. Chao Sun: Methodology, Validation, Investigation. Haijun Wu: Investigation, Supervision. Jizhen Xie: Investigation, Supervision. Tong Zhang: Investigation. Yumin Li: Investigation. Xuelian Xu: Investigation. Peilin Wang: Conceptualization, Supervision, Funding acquisition. Cheng Wang: Conceptualization, Writing – review & editing, Project administration, Supervision, Funding acquisition.

Declaration of competing interest

The authors declare that they have no known competing financial interests or personal relationships that could have appeared to influence the work reported in this paper.

Acknowledgments

This work was financially supported by National Natural Science Foundation of China (NSFC31872754), Fundamental Research Funds for the Central Universities (201964018) and Key Research and Development Program of Shandong Province (2015GSF121034).

Appendix A. Supplementary data

Supplementary data to this article can be found online at https://doi.org/10.1016/j.mtbio.2021.100189.

References

[1] H. Sung, J. Ferlay, R.L. Siegel, M. Laversanne, I. Soerjomataram, A. Jemal, F. Bray, Global cancer statistics 2020: GLOBOCAN estimates of incidence and mortality worldwide for 36 cancers in 185 countries, CA Cancer J Clin 71 (3) (2021) 209–249.

[2] J.A. Brockman, S. Alanee, A.J. Vickers, P.T. Scardino, D.P. Wood, A.S. Kibel, D.W. Lin, F.J. Bianco Jr., D.M. Rabah, E.A. Klein, J.P. Ciezki, T. Gao, M.W. Kattan, A.J. Stephenson, Nomogram predicting prostate cancer-specific mortality for men with biochemical recurrence after radical prostatectomy, Eur. Urol. 67 (6) (2015) 1160–1167.

[3] S. Sandhu, C.M. Moore, E. Chiong, H. Beltran, R.G. Bristow, S.G. Williams, Prostate cancer, Lancet 398 (2021) 1075–1090, 10305.

[4] R. de Wit, J. de Bono, C.N. Sternberg, K. Fizazi, B. Tombal, C. Wulfing, G. Kramer, J.C. Eymard, A. Bamias, J. Carles, R. Iacovelli, B. Melichar, A. Sverrisdottir, C. Theodore, S. Feyerabend, C. Helissey, A. Ozatilgan, C. Geffriaud-Ricouard, D. Castellano, C. Investigators, Cabazitaxel versus abiraterone or enzalutamide in metastatic prostate cancer, N. Engl. J. Med. 381 (26) (2019) 2506–2518.

[5] B.T. Rekoske, D.G. McNeel, Immunotherapy for prostate cancer: false promises or true hope? Cancer 122 (23) (2016) 3598–3607.

[6] K.G. Anderson, I.M. Stromnes, P.D. Greenberg, Obstacles posed by the tumor microenvironment to T cell activity: a case for synergistic therapies, Cancer Cell 31 (3) (2017) 311–325.

[7] G. Kroemer, L. Galluzzi, O. Kepp, L. Zitvogel, Immunogenic cell death in cancer therapy, Annu. Rev. Immunol. 31 (2013) 51–72.

[8] A.D. Garg, S. Martin, J. Golab, P. Agostinis, Danger signalling during cancer cell death: origins, plasticity and regulation, Cell Death Differ. 21 (1) (2014) 26–38.

[9] M. Obeid, A. Tesniere, F. Ghiringhelli, G.M. Fimia, L. Apetoh, J.L. Perfettini, M. Castedo, G. Mignot, T. Panaretakis, N. Casares, D. Metivier, N. Larochette, P. van Endert, F. Ciccosanti, M. Piacentini, L. Zitvogel, G. Kroemer, Calreticulin exposure dictates the immunogenicity of cancer cell death, Nat. Med. 13 (1) (2007) 54–61.

[10] F. Ghiringhelli, L. Apetoh, A. Tesniere, L. Aymeric, Y. Ma, C. Ortiz, K. Vermaelen, T. Panaretakis, G. Mignot, E. Ullrich, J.L. Perfettini, F. Schlemmer, E. Tasdemir, M. Uhl, P. Genin, A. Civas, B. Ryffel, J. Kanellopoulos, J. Tschopp, F. Andre, R. Lidereau, N.M. McLaughlin, N.M. Haynes, M.J. Smyth, G. Kroemer, L. Zitvogel, Activation of the NLRP3 inflammasome in dendritic cells induces IL-1beta-dependent adaptive immunity against tumors, Nat. Med. 15 (10) (2009) 1170–1178.

[11] L. Apetoh, F. Ghiringhelli, A. Tesniere, M. Obeid, C. Ortiz, A. Criollo, G. Mignot, M.C. Maiuri, E. Ullrich, P. Saulnier, H. Yang, S. Amigorena, B. Ryffel, F.J. Barrat, P. Saftig, F. Levi, R. Lidereau, C. Nogues, J.P. Mira, A. Chompret, V. Joulin, F. Clavel-Chapelon, J. Bourhis, F. Andre, S. Delaloge, T. Tursz, G. Kroemer, L. Zitvogel, Toll-like receptor 4-dependent contribution of the immune system to anticancer chemotherapy and radiotherapy, Nat. Med. 13 (9) (2007) 1050–1059.

[12] D.V. Krysko, A.D. Garg, A. Kaczmarek, O. Krysko, P. Agostinis, P. Vandenabeele, Immunogenic cell death and DAMPs in cancer therapy, Nat. Rev. Cancer 12 (12) (2012) 860–875.

[13] A. Gardner, A. de Mingo Pulido, B. Ruffell, Dendritic cells and their role in immunotherapy, Front. Immunol. 11 (2020) 924.

[14] N. Casares, M.O. Pequignot, A. Tesniere, F. Ghiringhelli, S. Roux, N. Chaput, E. Schmitt, A. Hamai, S. Hervas-Stubbs, M. Obeid, F. Coutant, D. Metivier, E. Pichard, P. Aucouturier, G. Pierron, C. Garrido, L. Zitvogel, G. Kroemer, Caspase-dependent immunogenicity of doxorubicin-induced tumor cell death, J. Exp. Med. 202 (12) (2005) 1691–1701.

[15] I. Vanmeerbeek, J. Sprooten, D. De Ruysscher, S. Tejpar, P. Vandenberghe, J. Fucikova, R. Spisek, L. Zitvogel, G. Kroemer, L. Galluzzi, A.D. Garg, Trial watch: chemotherapy-induced immunogenic cell death in immuno-oncology, OncoImmunology 9 (1) (2020).

[16] J. Lu, X. Liu, Y.P. Liao, F. Salazar, B. Sun, W. Jiang, C.H. Chang, J. Jiang, X. Wang, A.M. Wu, H. Meng, A.E. Nel, Nano-enabled pancreas cancer immunotherapy using immunogenic cell death and reversing immunosuppression, Nat. Commun. 8 (1) (2017) 1811.

[17] Z. Yu, J.F. Guo, M.Y. Hu, Y.Q. Gao, L.A. Huang, Icaritin exacerbates mitophagy and synergizes with doxorubicin to induce immunogenic cell death in hepatocellular carcinoma, ACS Nano 14 (4) (2020) 4816–4828.

[18] K. Sun, J. Hu, X. Meng, Y. Lei, X. Zhang, Z. Lu, L. Zhang, Z. Wang, Reinforcing the induction of immunogenic cell death via artificial engineered cascade bioreactor-enhanced chemo-immunotherapy for optimizing cancer immunotherapy, Small 17 (37) (2021), e2101897.

[19] V. Deretic, B. Levine, Autophagy balances inflammation in innate immunity, Autophagy 14 (2) (2018) 243–251.

[20] J. Doherty, E.H. Baehrecke, Life, death and autophagy, Nat. Cell Biol. 20 (10) (2018) 1110–1117.

[21] M. Michaud, I. Martins, A.Q. Sukkurwala, S. Adjemian, Y. Ma, P. Pellegatti, S. Shen, O. Kepp, M. Scoazec, G. Mignot, S. Rello-Varona, M. Tailler, L. Menger, E. Vacchelli, L. Galluzzi, F. Ghiringhelli, F. di Virgilio, L. Zitvogel, G. Kroemer, Autophagy-dependent anticancer immune responses induced by chemotherapeutic agents in mice, Science 334 (6062) (2011) 1573–1577.

[22] A. Fleming, T. Noda, T. Yoshimori, D.C. Rubinsztein, Chemical modulators of autophagy as biological probes and potential therapeutics, Nat. Chem. Biol. 7 (1) (2011) 9–17.

[23] B. Levine, N. Mizushima, H.W. Virgin, Autophagy in immunity and inflammation, Nature 469 (7330) (2011) 323–335.

[24] S.M. Ogbourne, A. Suhrbier, B. Jones, S.J. Cozzi, G.M. Boyle, M. Morris, D. McAlpine, J. Johns, T.M. Scott, K.P. Sutherland, J.M. Gardner, T.T. Le, A. Lenarczyk, J.H. Aylward, P.G. Parsons, Antitumor activity of 3-ingenyl angelate: plasma membrane and mitochondrial disruption and necrotic cell death, Cancer Res. 64 (8) (2004) 2833–2839.

[25] T.T. Le, J. Gardner, D. Hoang-Le, C.W. Schmidt, K.P. MacDonald, E. Lambley, W.A. Schroder, S.M. Ogbourne, A. Suhrbier, Immunostimulatory cancer chemotherapy using local ingenol-3-angelate and synergy with immunotherapies, Vaccine 27 (23) (2009) 3053–3062.

[26] L. Li, S. Shukla, A. Lee, S.H. Garfield, D.J. Maloney, S.V. Ambudkar, S.H. Yuspa, The skin cancer chemotherapeutic agent ingenol-3-angelate (PEP005) is a substrate for the epidermal multidrug transporter (ABCB1) and targets tumor vasculature, Cancer Res. 70 (11) (2010) 4509–4519.

[27] M. Yu, M.Q. Zhao, R.L. Yu, S.C. Chu, J.H. Xu, M. Xia, C. Wang, Nanotechnology-mediated immunochemotherapy with ingenol-3-mebutate for systematic anti-tumor effects, J. Contr. Release 304 (2019) 242–258.

[28] J. Shen, C. Sun, Z. Wang, Z. Chu, C. Liu, X. Xu, M. Xia, M. Zhao, C. Wang, Sequential receptor-mediated mixed-charge nanomedicine to target pancreatic cancer, inducing immunogenic cell death and reshaping the tumor microenvironment, Int. J. Pharm. 601 (2021) 120553.

[29] D. Fukurnura, J. Kloepper, Z. Amoozgar, D.G. Duda, R.K. Jain, Enhancing cancer immunotherapy using antiangiogenics: opportunities and challenges, Nat. Rev. Clin. Oncol. 15 (5) (2018) 325–340.

[30] C.H. Heldin, K. Rubin, K. Pietras, A. Ostman, High interstitial fluid pressure - an obstacle in cancer therapy, Nat. Rev. Cancer 4 (10) (2004) 806–813.

[31] T.C. Chou, P. Talalay, Quantitative analysis of dose-effect relationships: the combined effects of multiple drugs or enzyme inhibitors, Adv. Enzym. Regul. 22 (1984) 27–55.

[32] J. Ni, T. Miao, M. Su, N.U. Khan, X. Ju, H. Chen, F. Liu, L. Han, PSMA-targeted nanoparticles for specific penetration of blood-brain tumor barrier and combined therapy of brain metastases, J. Contr. Release 329 (2021) 934–947.

[33] J. Hrkach, D. Von Hoff, M. Mukkaram Ali, E. Andrianova, J. Auer, T. Campbell, D. De Witt, M. Figa, M. Figueiredo, A. Horhota, S. Low, K. McDonnell, E. Peeke, B. Retnarajan, A. Sabnis, E. Schnipper, J.J. Song, Y.H. Song, J. Summa, D. Tompsett, G. Troiano, T. Van Geen Hoven, J. Wright, P. LoRusso, P.W. Kantoff, N.H. Bander, C. Sweeney, O.C. Farokhzad, R. Langer, S. Zale, Preclinical development and clinical translation of a PSMA-targeted docetaxel nanoparticle with a differentiated pharmacological profile, Sci. Transl. Med. 4 (128) (2012), 128ra39.

[34] T. Qi, B. Chen, Z. Wang, H. Du, D. Liu, Q. Yin, B. Liu, Q. Zhang, Y. Wang, A pH-Activatable nanoparticle for dual-stage precisely mitochondria-targeted photodynamic anticancer therapy, Biomaterials 213 (2019) 119219.

[35] T. Barnoud, J.C. Leung, J.I. Leu, S. Basu, A.N.R. Poli, J.L.D. Parris, A. Indeglia, T. Martynyuk, M. Good, K. Gnanapradeepan, E. Sanseviero, R. Moeller, H.Y. Tang, J. Cassel, A.V. Kossenkov, Q. Liu, D.W. Speicher, D.I. Gabrilovich, J.M. Salvino, D.L. George, M.E. Murphy, A novel inhibitor of HSP70 induces mitochondrial toxicity and immune cell recruitment in tumors, Cancer Res. 80 (23) (2020) 5270–5281.

[36] Y.C. Sung, P.R. Jin, L.A. Chu, F.F. Hsu, M.R. Wang, C.C. Chang, S.J. Chiou, J.T. Qiu, D.Y. Gao, C.C. Lin, Y.S. Chen, Y.C. Hsu, J. Wang, F.N. Wang, P.L. Yu, A.S. Chiang, A.Y. Wu, J.J. Ko, C.P. Lai, T.T. Lu, Y. Chen, Delivery of nitric oxide with a nanocarrier promotes tumour vessel normalization and potentiates anti-cancer therapies, Nat. Nanotechnol. 14 (12) (2019) 1160–1169.